Research Square

Preprints are preliminary reports that have not undergone peer review.
They should not be considered conclusive, used to inform clinical practice,
or referenced by the media as validated information.

Alignment of methylcellulose nanofibrils through confinement

Aref Ghaemi

aref.ghaemi@aalto.fi

Aalto University

Maryam Roza Yazdani McCord

Aalto University

Tero Mäkinen

Aalto University

Juha Koivisto

Aalto University

Mikko Alava

Aalto University

Research Article

Keywords:

Posted Date: November 25th, 2026

DOI: https://doi.org/10.21203/rs.3.rs-11757846/v1

License: This work is licensed under a Creative Commons Attribution 4.0 International License.
Read Full License

Additional Declarations: No competing interests reported.

Cellulose manuscript No.
(will be inserted by the editor)

Alignment of methylcellulose nanofibrils through confinement

Aref Ghaemi (Corresponding author) · Maryam Roza Yazdani McCord · Tero Mäkinen · Juha Koivisto · Mikko Alava

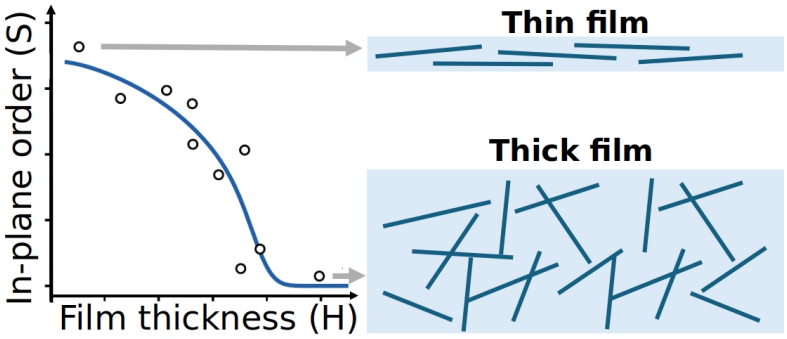
Received: date / Accepted: date

Abstract In wood, cellulose microfibrils are organized within the thin layers of the cell wall, where their alignment largely determines the mechanical behavior of the fiber. Here we observe thickness-dependent alignment in dried methylcellulose films and show that a confinement-based model captures this trend. Methylcellulose forms nanofibrils on thermal gelation, and in foams these fibrils dry within the thin films that separate the bubbles. Using scanning electron microscopy and image-based orientation analysis, we find that methylcellulose nanofibrils in foam films are strongly aligned in the film plane, whereas fibrils in bulk-dried hydrogels are nearly isotropic. The degree of alignment decreases with film thickness: the in-plane order parameter, which ranges from 0 for random to 1 for perfect alignment, falls from about 0.7 in films of roughly 100 nm to near zero in films thicker than about 800 nm. A reduced statistical-mechanical model, in which confinement restricts the out-of-plane tilt of rod-like fibrils and thereby strengthens their in-plane excluded-volume interactions, reproduces this decrease with two fitted parameters. The results identify film thickness as a simple processing variable for controlling nanofibril orientation in bio-based foams, and provide a qualitative synthetic analogue of microfibril organization in natural cell walls.

Keywords methylcellulose · nanofibrils · confinement · orientational order · foam films · bio-based foams

A. Ghaemi · M.R. Yazdani McCord · T. Mäkinen · J. Koivisto · M. Alava
Department of Applied Physics, Aalto University, Konemiehentie 1, 02150 Espoo, Finland
E-mail: aref.ghaemi@aalto.fi

Graphical abstract



Methylcellulose nanofibrils dried in thin foam films align in the film plane. The degree of alignment reduces with film thickness, from significant alignment measured by the in-plane nematic order parameter at 100 nm to isotropy above about 800 nm. A confinement model, in which thinner films restrict fibril tilt and strengthen in-plane excluded-volume interactions, reproduces this trend.

Introduction

Wood fibers owe much of their stiffness and strength to the organization of their cell walls (Bergander and Salmén 2002; Cave and Walker 1994). The S2 layer of the secondary wall makes up about 80% of the wall thickness and consists of aggregates of cellulose microfibrils arranged in concentric lamellae (Booker and Sell 1998; Fahlén and Salmén 2005). Within this layer, the microfibrils wind helically around the fiber axis (see Fig. 1a), and both the microfibril angle (MFA) and its spread largely set the axial stiffness of the fiber (Cave and Walker 1994; Barnett and Bonham 2004). In softwoods, the MFA decreases from about 30° in earlywood to about 5° in latewood, together with a narrower angular distribution (Anagnost et al. 2002; Barnett and Bonham 2004).

How this order arises is only partly understood. In living cells, cellulose synthase complexes move along tracks defined by cortical microtubules, which guide the direction in which microfibrils are deposited (Paredez et al. 2006). Geometrical models add that the shape of the cell and the space available for deposition constrain the resulting helix (Emons et al. 2002). Physics suggests a simpler contribution: rod-like particles crowded into a thin layer lose orientational freedom out of the plane and order spontaneously within it (Onsager 1949; van Roij et al. 2000; Dijkstra et al. 2001). Whether confinement

alone can produce cell-wall-like order in a cellulose-based system has not been explicitly demonstrated.

Methylcellulose (MC) is a convenient system for such a test. Replacing hydroxyl groups of cellulose with methoxy groups makes MC water-soluble, and on heating its chains assemble into nanofibrils as the solution gels (Bodvik et al. 2010; Lott et al. 2013; Coughlin et al. 2021). The fibrils are about 15–20 nm wide (Lott et al. 2013; Schmidt et al. 2018) and bundle into structures that remain stiff over micrometre lengths (Rosenmann et al. 2026), so on the scale of a thin film they behave as rod-like objects. In the bulk, these bundles form a network with no preferred orientation (Rosenmann et al. 2026). Although the gelation mechanism is still debated (Coughlin et al. 2021; Morozova 2020; Ginzburg et al. 2016; Miranda-Valdez et al. 2026), the fibrils provide cellulose-derived building blocks whose organization can be examined after drying.

Foams offer a scalable way to produce useful materials in which these fibrils are confined in thin sheets. MC foams can be produced at large scale and are often strongly anisotropic (Reichler et al. 2021; Miranda-Valdez et al. 2023b,a; Mobredi et al. 2024; Mac Intyre et al. 2022). Their bubble walls are thin films whose thickness varies from place to place, so a single foam samples a range of confinements. Salt provides a second route: salts alter the fibrillar structure of MC gels (Liberman et al. 2021), and, as we show below, salt-containing hydrogels dry into stacked layers that also confine the fibrils. Orientation in cellulose-based foams has so far been attributed to other mechanisms: pulp fibers align with elongated bubbles in foam-formed materials (Reichler et al. 2021), ice templating aligns nanocellulose in freeze-cast foams (Wicklein et al. 2015), and MC–cellulose nanocrystal hydrogels and fibers show tunable birefringence (Hynninen et al. 2018, 2021). More generally, cellulose nanofibrils and nanocrystals are aligned by flow, external fields or chemically triggered gelation to obtain direction-dependent mechanical, optical and thermal properties (Li et al. 2021; Håkansson et al. 2014; Hausmann et al. 2020; Wise et al. 2020). In all of these cases, a process imposes alignment on pre-formed particles; whether the thickness of the sheet in which fibrils assemble can by itself set their order has not been examined.

In this work, we use scanning electron microscopy (SEM) and structure-tensor orientation analysis to measure the in-plane order of MC nanofibrils in foam films (Fig. 1b), salt-induced layers and bulk-dried hydrogels. Among the samples examined, pronounced fibril alignment occurs in thin sheets, and the measured order generally decreases with sheet thickness. We rationalize this with a reduced Onsager-type model: in a thinner film, fibrils can tilt less out of the plane, which strengthens their in-plane excluded-volume interactions and drives alignment. With two fitted parameters, an interaction strength and an effective fibril length, the model reproduces the observed loss of order with thickness. To our knowledge, this is the first report of confinement-induced alignment of MC nanofibrils and of its dependence on film thickness. The films thus offer a qualitative synthetic counterpart to the thin lamellae in which microfibrils are organized in natural fiber walls.

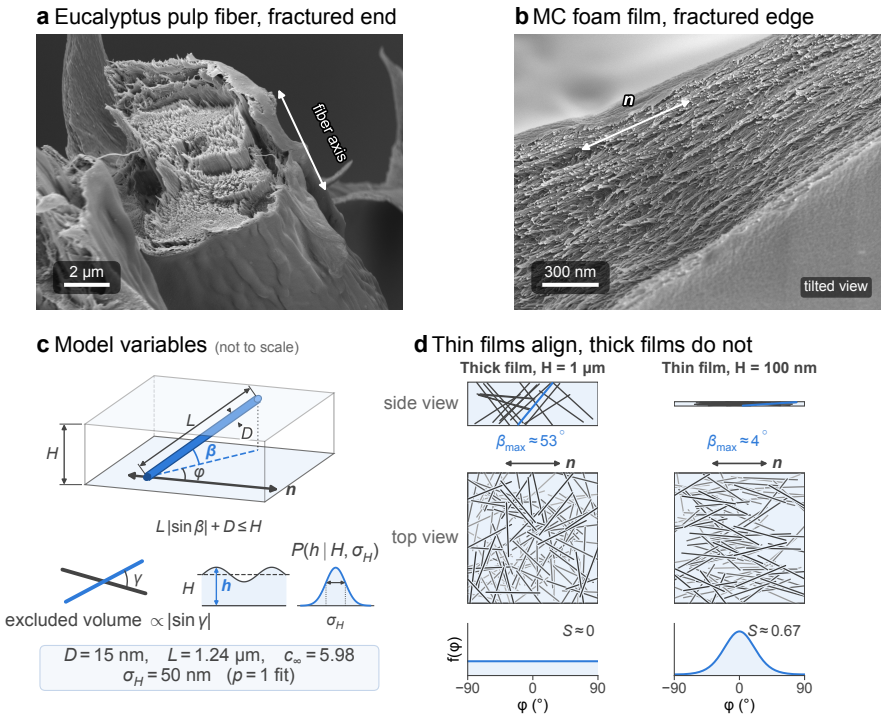


Fig. 1 Confinement as a route to cell-wall-like fibril order. **a** Fractured end of a eucalyptus pulp fiber in an MC/pulp foam, showing cellulose microfibril bundles protruding from the layered cell wall; the arrow marks the fiber axis. **b** Fractured edge of a methylcellulose foam film (tilted view), showing nanofibrils lying in the film plane and oriented predominantly along a common director **n**. Micrographs are shown as recorded by the instrument, without processing other than annotation. **c** Variables of the confinement model (not to scale). A fibril is a rigid rod of length L and diameter D in a film of thickness H, oriented by its out-of-plane tilt β and its in-plane angle φ relative to **n**. The rod is drawn at maximum tilt, where it touches both film surfaces. Rods interact through their excluded volume, which depends on the angle γ between them, and the local film thickness h varies about its mean H with standard deviation σ_H. **d** Schematic comparison of a thick ($H = 1$ μm) and a thin ($H = 100$ nm) film. Side views (top row) show the tilt allowed by confinement; top views (middle row) show rods of length L with in-plane angles drawn from the distributions in the bottom row. Rod shading indicates height within the film (lighter rods lie lower), so overlapping rods lie at different heights rather than intersecting. Fibrils in the thick film are randomly oriented ($S \approx 0$), whereas those in the thin film align along **n** ($S \approx 0.67$; $S = 0$ for random and 1 for perfect alignment). Side and top views are drawn to the same length scale.

Materials and Methods

Materials

Methylcellulose (Benecel™ MX MC-50000) was obtained from Ashland Specialties Belgium, and sodium chloride (NaCl, ACS reagent, $\geq$ 99.0%) from Merck. Like other MC grades, this grade forms a thermoreversible gel on heating. However, it gels at about 40 °C rather than the 50–60 °C typical of regular grades, and its gel retains its firmness on cooling to about 38–40 °C, whereas gels of regular grades revert to solution (Ashland 2019). A 2 wt% aqueous solution of this grade has a nominal viscosity of 50 Pa·s (Ashland 2019), and the grade has a weight-average molecular weight of 534 $\mathrm{kg\,mol^{-1}}$, a degree of substitution (DS) of 1.87 and an intrinsic viscosity of 1351 $\mathrm{mL\,g^{-1}}$ at 25 °C (Miranda-Valdez et al. 2024). Ultrapure water (Milli-Q) was used throughout.

Sample preparation

MC solutions of 1.5 wt% were prepared by dispersing MC powder in one third of the water at 80 °C and stirring for 10 min; the remaining water, at room temperature, was then added and the solution stirred for another 10 min before being cooled in an ice bath under stirring for 1 h. Solutions were stored at 3 °C for at least 24 h before use. For salt-containing samples, NaCl (1.5 wt%) was dissolved in the hot water before the MC powder was added.

Bulk hydrogels were cast in aluminium weighing dishes (57 mm in diameter; 40 g of solution) and dried at 80 °C, above the gelation temperature, until constant mass. Without salt, the gels dried into compact solids; with NaCl, they dried into stacked layers.

Foams were prepared by the Tessari method (Tessari et al. 2001): air and MC solution were pumped back and forth between two 60-mL syringes connected by a tube, at an air-to-liquid ratio of 1:1, for 5 to 10 passes until a stable foam formed. The foam was extruded onto a Teflon-coated sheet and dried under a heat lamp for about 12 h at a surface temperature of about 50 °C, above the gelation temperature. The dried foam sheets were 2–5 mm thick. In addition, freeze-dried foams that were prepared from gelled MC solutions, and in which nanofibril alignment was also observed, are described in Supplementary Information, Section S2.

The pulp fiber shown in Fig. 1a was imaged in a foam containing 1.5 wt% MC and 1.5 wt% eucalyptus kraft pulp fibers (CMPC, bleached). Pulp sheets were soaked in water and mechanically sheared until a fiber slurry formed. The slurry was then used in place of the room-temperature water in the MC solution preparation described above, i.e. added to the hot MC dispersion. The suspension was foamed by the Tessari method, and the foam was dried and imaged in the same way as the other samples.

Scanning electron microscopy

Samples were fractured by hand at room temperature, mounted on aluminium stubs with carbon tape and coated with 4 nm of platinum (Leica EM ACE600). Imaging used a Zeiss Sigma VP microscope with an in-lens secondary-electron detector at 2–4 kV and a working distance of 4–5 mm. Images for orientation analysis were recorded on fracture surfaces at 10–30 kX (pixel size 5.729–1.910 nm), with 5 images per sample. Pixel sizes were taken from the calibration stored in each image file.

Film thickness

The thickness H of each analyzed film was measured in Fiji (Schindelin et al. 2012) from SEM images of the film's fractured edge viewed edge-on, as the mean of 5 measurements along the edge. Local thickness variation was quantified from the same measurements as a standard deviation, $\sigma_H = 50$ nm, which was used in the thickness-averaged model.

Orientation analysis

In-plane fibril orientations were quantified with the OrientationJ Distribution plugin in Fiji (Rezakhaniha et al. 2012), which estimates local orientation and coherence from the image structure tensor. Gradients were computed with the cubic-spline method. Following the recommendation of the plugin authors, the standard deviation σ of the Gaussian window was set separately for each image so that it matched the size of the studied feature in pixels. The window therefore spanned approximately the fibril width (15 nm) in every image, which keeps the analysis at a fixed physical scale and makes the resulting order parameters comparable across magnifications. The plugin returns a histogram of in-plane angles over the whole image, which was normalized and used to calculate the in-plane order parameter

$$S = \left|\langle e^{2i\phi}\rangle\right| = \langle \cos 2(\phi - \phi_0)\rangle, \tag{1}$$

where ϕ is the in-plane orientation angle and ϕ_0 the mean director. S is 0 for an isotropic distribution and 1 for perfect alignment.

Eight foam samples were prepared independently from the same MC grade, and more than 30 images were recorded on each at different magnifications, of which more than 10 per sample resolved individual nanofibrils. Each data point in Fig. 3 corresponds to one image of one film, for which S and H were measured together, since the analysis requires a single film of uniform thickness within the analyzed region. Images were included when the fracture surface of a single film lay approximately parallel to the imaging plane, its full width was visible for the thickness measurement, and individual fibrils were resolved; this gave 10 films from the 8 samples, with one or two films per sample. The

cast hydrogels, with and without NaCl, were prepared as three samples each, with more than 30 images per sample. For all samples, SEM measures only the projected, in-plane orientation of the fibrils; their out-of-plane order is therefore not measured directly but inferred from the model.

Model calculations

The confinement model is introduced in the Results. Its self-consistent equation was solved on a grid of 72 azimuthal and 61 tilt angles by damped fixed-point iteration. The interaction strength c_∞ and effective fibril length L were obtained by minimizing the sum of squared residuals between predicted and measured S for the 10 films, using differential evolution followed by local refinement. The fibril diameter was fixed at $D = 15$ nm (Rosenmann et al. 2026), and σ_H at the measured value. Grid convergence, branch selection, sensitivity to D and σ_H, and residual-bootstrap confidence intervals are reported in Supplementary Information, Sections S1.2.2, S1.2.3, S1.3.2 and S1.3.4, respectively.

Fibril length measurement

Fibril contour lengths were measured from SEM images of foam films by automated skeleton tracing in Python (scikit-image 0.25.2, Van der Walt et al. (2014)). Images were cropped to the fibrillar film region. After background flattening and local contrast normalization, fibrils were enhanced with a multiscale ridge filter (Sato) at scales set from the fibril width (15 nm), thresholded (Otsu) and skeletonised. Side branches shorter than 40 nm were pruned, the skeleton was split into unbranched segments at junctions, and segment contour lengths were converted to nanometres using the pixel size from the instrument metadata of each original image. Regions outside the film, including padding from cropping, were excluded, and segments within 50 nm of the region boundary were treated as truncated. Segments shorter than 50 nm, and segments whose end-to-end distance was less than 0.7 of their contour length, were discarded, since curled traces typically jump between neighboring fibrils. Because fibrils overlap and cross, traced lengths are bounded above by the true fibril length; the longest traced segments of each image were therefore used for comparison with the fitted L. Varying the threshold by $\pm 20\%$ and the pruning length between 20 and 80 nm changed the pooled 99th percentile of traced lengths between 0.55 and 0.90 μm (0.73 μm at default settings), and in any setting at most six segments exceeded the longer of the two fitted fibril lengths ($L = 1.24$ μm; see Results). Stage tilts of up to 14° foreshorten projected lengths by at most 3% and were not corrected.

Results and Discussion

Figure 2 compares the fibril arrangement in the three dried materials. In the bulk-dried hydrogel without salt (Fig. 2a), nanofibrils form a disordered network, and the orientation distribution is nearly flat ($S = 0.03$). With NaCl, the gel dried into stacked layers (Fig. 2b), within which fibrils share a preferred direction ($S = 0.57$). In the thin films separating the bubbles of the dried foam (Fig. 2c), fibrils lie in the film plane and are clearly aligned ($S = 0.41$ in a film of $H \approx 718$ nm). Alignment thus appears only where the material is a thin sheet, whether the sheet is a bubble wall or a salt-induced layer. Freeze-dried foams, in which the walls form without evaporative drying, also showed aligned fibrils (Supplementary Information, Section S2 and Fig. S10). This shows that alignment also occurs through a preparation route without evaporative drying, although freezing introduces additional structure-forming processes and therefore does not isolate confinement.

Order falls with film thickness

Because the bubble walls of a single foam vary in thickness, the foam samples a range of confinements. Orientation distributions measured on films of different thickness are shown in Fig. 2d. Thin films give narrow distributions, which broaden as the films become thicker. The corresponding order parameters (Fig. 3) decrease from about 0.7 at $H \approx 100$ nm to near zero at $H \approx 1$ μm, with most of the loss occurring between about 600 and 800 nm. Films with similar measured thickness can have substantially different order parameters. Local thickness variation, differences between the thickness and orientation measurement regions, and other structural heterogeneity may contribute to this scatter.

Confinement reproduces the trend

To examine whether restricting out-of-plane fibril orientations can reproduce this trend, we use a reduced statistical-mechanical model in which film thickness limits the out-of-plane tilt of rod-like fibrils (Fig. 1c); the full derivation is given in Supplementary Information, Section S1.1. A fibril is a rigid rod of length L and diameter D, oriented by its in-plane angle φ and its tilt β out of the film plane. A rod fits in a film of thickness H only if

$$L\,|\sin\beta| + D \le H, \tag{2}$$

so that the largest accessible tilt is $\sin\beta_{\max} = (H - D)/L$. Weighting each tilt by its orientational phase space and by the vertical room left for the rod's centre gives the tilt distribution

$$q_H(\beta) \propto \cos\beta\ \left[H - D - L\,|\sin\beta|\right]_+ , \tag{3}$$

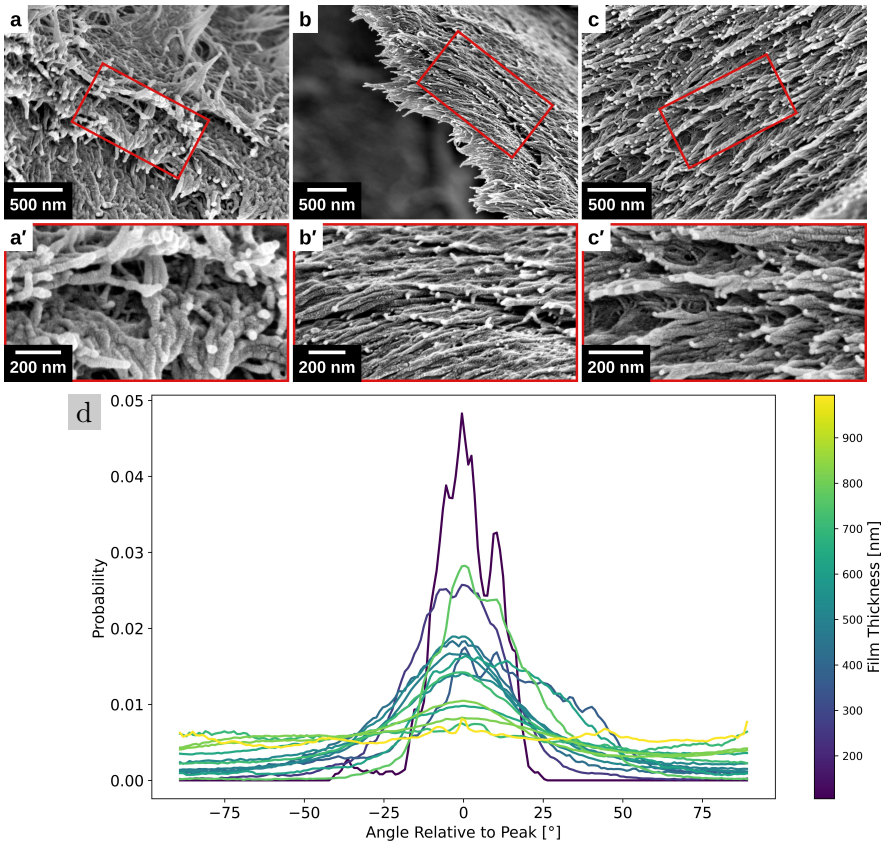


Fig. 2 Nanofibril alignment in dried MC materials. **a** Bulk-dried MC hydrogel without salt, with a disordered fibril network. **b** Bulk-dried MC hydrogel containing NaCl, which dried into stacked layers with aligned fibrils. **c** Thin film of a dried MC foam, with clearly aligned fibrils. **a′**–**c′** Enlarged views of the regions marked by red boxes in **a**–**c**, which were used for the analysis; each region is rotated so that the dominant fibril direction runs horizontally. **d** In-plane orientation distributions measured on foam films of different thickness, colored by film thickness and aligned at their peaks. Thinner films give narrower distributions.

where $[x]_+ = \max(x, 0)$. Thinner films therefore confine fibrils closer to the film plane.

Pairs of rods interact through an angular kernel $|\sin\gamma|^p$, where γ is the angle between them. The case $p = 1$ is the angular dependence of the excluded volume of slender hard rods (Onsager 1949); $p = 2$ is a smoother, quadratic alternative which is simply there to test how far the conclusions depend on the assumed interaction law. These interactions act only on the in-plane orientation: the tilt distribution is taken from the confinement geometry of a single

rod, and any change to it caused by interactions between fibrils is neglected. Since SEM resolves only in-plane orientations, the kernel is averaged over the tilts of both rods,

$$\bar{K}_p(\Delta\varphi; H) = \iint q_H(\beta)\, q_H(\beta')\, |\sin\gamma|^p \,\mathrm{d}\beta\,\mathrm{d}\beta', \tag{4}$$

with $\cos\gamma = \cos\beta\cos\beta'\cos\Delta\varphi + \sin\beta\sin\beta'$. When fibrils lie flat, γ equals the in-plane angle difference and in-plane misalignment is penalized most strongly; tilted rods dilute this penalty. Minimizing an Onsager-type free energy gives the self-consistent in-plane distribution

$$f_H(\varphi) \propto \exp\left[-c_\infty \int_0^\pi f_H(\varphi')\, \bar{K}_p(\varphi - \varphi'; H)\,\mathrm{d}\varphi'\right], \tag{5}$$

where c_∞ sets the strength of the interaction relative to orientational entropy, and S follows from Eq. (1). Film thickness enters only through the accessible tilts, so the thickness dependence of S is not imposed but follows from the confinement geometry. To account for local thickness variation within each analyzed region, the prediction is averaged over a Gaussian distribution of local thicknesses h of width σ_H,

$$S_{\mathrm{obs}}(H) = \int S(h)\, P(h \mid H, \sigma_H)\,\mathrm{d}h. \tag{6}$$

This average assumes that regions of different local thickness share a common in-plane director; if the director varied across the image, the measured order parameter would be lower still. Branch tracking across the ordering transition, which confirms that the loss of order at large H is an equilibrium result rather than a numerical artifact, is described in Supplementary Information, Section S1.2.3.

With $D = 15$ nm and $\sigma_H = 50$ nm fixed, c_∞ and L were fitted to the ten films separately for each kernel (Fig. 3). The $p = 1$ kernel gives $c_\infty = 5.98$ [95% CI: 5.52–7.05] and $L = 1.24$ μm [95% CI: 0.81–1.77 μm] with $R^2 = 0.83$, and the $p = 2$ kernel gives $c_\infty = 5.38$ [95% CI: 4.96–7.62] and $L = 0.80$ μm [95% CI: 0.38–0.97 μm] with $R^2 = 0.81$ (Supplementary Information, Section S1.3.4 and Table S4). In both cases the two parameters are correlated, since a longer rod and a weaker interaction shift the transition in the same way. Moreover, H is the thickness of the dried film, whereas fibril order may develop before drying is complete. The fit therefore assumes that the dry thickness reflects the relative confinement during structure formation, and L should be read as an effective, confinement-relevant length rather than as the length of individual fibrils. The two kernels reproduce the loss of order with thickness almost equally well, so the result does not hinge on the exact form of the interaction. We use $P = 1$ as the primary model because it retains the angular dependence of the excluded volume of slender rods. The $P = 2$ model gives

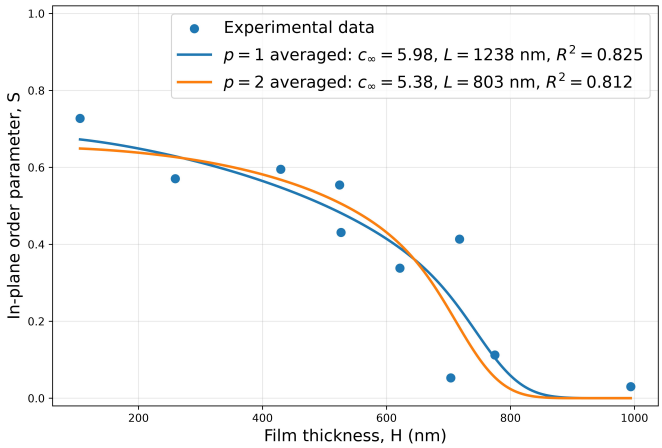


Fig. 3 In-plane order parameter S of MC nanofibrils as a function of film thickness H. Symbols: measured films. Lines: confinement model averaged over local thickness variation ($\sigma_H = 50$ nm), with the excluded-volume kernel $p = 1$ and the quadratic kernel $p = 2$. Both kernels reproduce the loss of order with thickness.

a similar thickness dependence, indicating that the qualitative trend is not specific to the chosen kernel (Supplementary Information, Section S1.3.2 and Table S3).

We compared the fitted effective length with traceable fibrillar structures in SEM images as an order-of-magnitude consistency check: if the fitted length did not correspond to the fibrils actually present in the films, the agreement in Fig. 3 would reflect curve fitting rather than confinement. We therefore measured fibril lengths directly from SEM images by skeleton tracing (Supplementary Information, Section S3 and Figs. S11–S12). Tracing is biased in two opposite ways: where fibrils overlap and cross, a single fibril is broken into several shorter segments, so traced lengths are generally lower bounds; where fibrils are highly aligned, fibrils lying end to end can merge into a single, longer trace. The relevant observable is therefore the length of the longest traceable segments rather than the mean. In seven of the eight images analyzed, the longest traced segments were 0.55–1.15 μm long (median 0.69 μm), and the length distributions fell off steeply above this range. The longest traceable structures are thus of the same order as the fitted lengths (0.80 μm for $p = 2$ and 1.24 μm for $p = 1$), as the mechanism requires; being lower bounds, they do not discriminate between the two kernels. In the remaining image, of a highly aligned film surface, segments of up to 2.5 μm were traced along surface grooves, and given the merging of aligned fibrils these are upper estimates.

Salt, flow and drying

The salt-containing hydrogels show that confinement does not require bubbles. Salts alter the fibrillar structure of MC gels (Liberman et al. 2021), and with NaCl the gels dried into stacked layers within which fibrils were aligned. The lower order in these layers than in the thinnest foam films is consistent with thicker layers, although the layer thickness was not measured.

The model is symmetric within the film plane: it predicts how sharply fibrils align, but not along which direction. The direction must therefore be selected by something else. In the foams, extensional flow during extrusion through the syringe tube and drainage within the films can provide a common direction; the salt layers, dried at rest in an aluminum weighing dish, had no imposed flow. Because S is averaged over each image, regions with different local directions lower the measured order even when each region is well aligned, which may contribute to the lower S of the salt layers.

During drying, depletion attraction and capillary forces can also bring fibrils together and align them (Thorkelsson et al. 2015), and their relative importance would depend on whether fibrils form before or during evaporation, which for MC can occur within milliseconds under mechanical impact (Parvari et al. 2018). The reduced model reproduces the observed thickness dependence without explicitly including these forces. It also treats the dried structure as an equilibrium state, although the structure forms out of equilibrium as the film dries. This demonstrates the plausibility of a confinement-based explanation, but does not establish which mechanisms dominate during film formation, or whether the final arrangement retains features of the drying path.

Comparison with natural fiber walls

The pulp fiber in Fig. 1a shows the arrangement that motivated this work: in the S2 layer, cellulose microfibril aggregates are organized in thin concentric lamellae (Booker and Sell 1998; Fahlén and Salmén 2005). The MC films reproduce this qualitative picture, with fibrils ordered within a thin layer and more strongly the thinner the layer. The separation between direction and sharpness suggested by the model has a natural counterpart in the cell wall. There, the direction of deposition is guided by cortical microtubules (Paredez et al. 2006), much as flow can select the direction in the foams, while confinement within a lamella could contribute to how narrowly the microfibrils are distributed about that direction. The comparison is qualitative: cell-wall microfibrils are crystalline and deposited by an active process, whereas MC fibrils self-assemble in a drying film. It does, however, suggest a testable link between lamella thickness and the spread of the microfibril angle in wood.

Conclusions

MC nanofibrils align where the material dries as a thin sheet. In the thin films separating foam bubbles and in the layers formed by salt-containing hydrogels, fibrils share a common in-plane direction, whereas in bulk-dried hydrogels they form an isotropic network. In foam films, the in-plane order parameter decreases with film thickness, from about 0.7 in films of roughly 100 nm to near isotropy above about 800 nm.

A reduced Onsager-type model, in which film thickness limits the out-of-plane tilt of rod-like fibrils and thereby strengthens their in-plane excluded-volume interactions, reproduces this decrease with two parameters, an interaction strength and an effective fibril length. The result is insensitive to the exact form of the interaction kernel, and the fitted fibril length is of the same order as the longest fibrils traced in SEM images. The model shows that confinement-induced restriction of fibril tilt can account for the observed thickness dependence. The experiments are consistent with this mechanism, while allowing contributions from flow and forces acting during drying. Flow during extrusion or drainage may also help select the alignment direction.

These findings identify film thickness as a promising processing variable for tuning nanoscale anisotropy in bio-based foams. Since only one MC grade and one salt were studied, extending the comparison to other grades and salts, which alter the fibrillar structure of MC gels, would test how general this relation is. In other fibrillar systems, aligning rod-like particles produces strongly direction-dependent mechanical properties. In foams, nanofibril alignment within the walls could therefore contribute to mechanical anisotropy alongside the shape and orientation of the cells, provided the fibril directions are coordinated across walls, for example by extrusion. Separating these two contributions is a question for future work. The MC films also offer a qualitative synthetic counterpart to the thin lamellae of natural fiber walls, and suggest that confinement within a lamella could contribute to how narrowly cell-wall microfibrils are distributed about their direction. This hypothesis could be tested in wood by relating lamella thickness to the spread of the microfibril angle.

Acknowledgements

M.J.A., T.M., and J.K. acknowledge funding from the FinnCERES flagship (151830423), Business Finland (210129, 211835, 211909, 211989), and the Future Makers program. A.G. and M.J.A. would like to acknowledge funding received from Suomen Kulttuurirahasto. T. M. acknowledges funding from the Research Council of Finland (130265). A.G., J.K., T.M., and M.J.A. acknowledge funding from EU: ARCHIBIOFOAM project has received funding from the European Union's Horizon Europe research and innovation programme under grant agreement No 101161052. Views and opinions expressed are however those of the author(s) only and do not necessarily reflect those of the Eu-

ropean Union or European Innovation Council and SMEs Executive Agency (EISMEA). Neither the European Union nor the granting authority can be held responsible for them.

Author contributions

Aref Ghaemi: Conceptualization, Methodology, Investigation, Formal analysis, Software, Visualization, Writing – original draft. Maryam Roza Yazdani, Tero Mäkinen, and Juha Koivisto: Writing – review & editing. Mikko Alava: Supervision, Funding acquisition, Writing – review & editing. All authors read and approved the final manuscript.

Competing interests

The authors declare no competing interests.

Data availability

The numerical model, fitting pipeline, verification analyses, fibril-tracing code and the data supporting the findings of this study are available from the corresponding author upon reasonable request.

References

Anagnost SE, Mark RE, Hanna RB (2002) Variation of microfibril angle within individual tracheids. Wood and fiber science pp 337–349

Ashland (2019) Benecel™ MX modified cellulose for plant based foods. Product sell sheet HW19-008.1, Ashland, Wilmington, DE, accessed 2 November 2026

Barnett JR, Bonham VA (2004) Cellulose microfibril angle in the cell wall of wood fibres. Biological reviews 79(2):461–472

Bergander A, Salmén L (2002) Cell wall properties and their effects on the mechanical properties of fibers. Journal of materials science 37(1):151–156

Bodvik R, Dedinaite A, Karlson L, Bergström M, Bäverbäck P, Pedersen JS, Edwards K, Karlsson G, Varga I, Claesson PM (2010) Aggregation and network formation of aqueous methylcellulose and hydroxypropylmethylcellulose solutions. Colloids and Surfaces A: Physicochemical and Engineering Aspects 354(1-3):162–171

Booker R, Sell J (1998) The nanostructure of the cell wall of softwoods and its functions in a living tree. Holz als Roh-und Werkstoff 56(1):1–8

Cave I, Walker J (1994) Stiffness of wood in fast-grown plantation softwoods: the influence of microfibril angle. Forest products journal 44(5):43

Coughlin ML, Liberman L, Ertem SP, Edmund J, Bates FS, Lodge TP (2021) Methyl cellulose solutions and gels: Fibril formation and gelation properties. Progress in Polymer Science 112:101324

Dijkstra M, van Roij R, Evans R (2001) Wetting and capillary nematization of a hard-rod fluid: A simulation study. Physical review E 63(5):051703

Emons A, Schel J, Mulder B (2002) The geometrical model for microfibril deposition and the influence of the cell wall matrix. Plant Biology 4(01):22–26

Fahlén J, Salmén L (2005) Pore and matrix distribution in the fiber wall revealed by atomic force microscopy and image analysis. Biomacromolecules 6(1):433–438

Ginzburg VV, Sammler RL, Huang W, Larson RG (2016) Anisotropic self-assembly and gelation in aqueous methylcellulose—theory and modeling. Journal of Polymer Science Part B: Polymer Physics 54(16):1624–1636

Håkansson KM, Fall AB, Lundell F, Yu S, Krywka C, Roth SV, Santoro G, Kvick M, Prahl Wittberg L, Wågberg L, et al. (2014) Hydrodynamic alignment and assembly of nanofibrils resulting in strong cellulose filaments. Nature communications 5(1):4018

Hausmann MK, Siqueira G, Libanori R, Kokkinis D, Neels A, Zimmermann T, Studart AR (2020) Complex-shaped cellulose composites made by wet densification of 3d printed scaffolds. Advanced Functional Materials 30(4):1904127

Hynninen V, Hietala S, McKee JR, Murtomäki L, Rojas OJ, Ikkala O, Nonappa (2018) Inverse thermoreversible mechanical stiffening and birefringence in a methylcellulose/cellulose nanocrystal hydrogel. Biomacromolecules 19(7):2795–2804

Hynninen V, Patrakka J, Nonappa (2021) Methylcellulose–cellulose nanocrystal composites for optomechanically tunable hydrogels and fibers. Materials 14(18):5137

Li K, Clarkson CM, Wang L, Liu Y, Lamm M, Pang Z, Zhou Y, Qian J, Tajvidi M, Gardner DJ, et al. (2021) Alignment of cellulose nanofibers: harnessing nanoscale properties to macroscale benefits. ACS nano 15(3):3646–3673

Liberman L, Schmidt PW, Coughlin ML, Ya'akobi AM, Davidovich I, Edmund J, Ertem SP, Morozova S, Talmon Y, Bates FS, et al. (2021) Salt-dependent structure in methylcellulose fibrillar gels. Macromolecules 54(5):2090–2100

Lott JR, McAllister JW, Arvidson SA, Bates FS, Lodge TP (2013) Fibrillar structure of methylcellulose hydrogels. Biomacromolecules 14(8):2484–2488

Mac Intyre JR, Raka D, Aydin M, Viitanen L, Koivisto J (2022) Measuring biofoam anisotropy using optical coherence tomography. Journal of Materials Science 57(25):11663–11672

Miranda-Valdez IY, Coffeng S, Zhou Y, Viitanen L, Hu X, Jannuzzi L, Puisto A, Kostiainen MA, Mäkinen T, Koivisto J, et al. (2023a) Foam-formed biocomposites based on cellulose products and lignin. Cellulose 30(4):2253–2266

Miranda-Valdez IY, Yazdani MR, Mäkinen T, Coffeng S, Viitanen L, Koivisto J, Alava MJ (2023b) Cellulose foams as scalable templates for phase change materials. Journal of Energy Storage 73:109036

Miranda-Valdez IY, Puente-Córdova JG, Rentería-Baltiérrez FY, Fliri L, Hummel M, Puisto A, Koivisto J, Alava MJ (2024) Viscoelastic phenomena in methylcellulose aqueous systems: Application of fractional calculus. Food Hydrocolloids 147:109334

Miranda-Valdez IY, Puente-Córdova JG, Mäkinen T, Koivisto J, McKinley GH, Alava MJ (2026) Fractional rheology of methylcellulose thermogelation. Journal of Rheology 70(6):1363–1381

Mobredi K, Miranda-Valdez IY, Mäkinen T, Koivisto J, Alava MJ (2024) A simple approach to produce hydrophobic biobased coatings using methylcellulose and organosolv lignin. Soft Matter 20(28):5607–5615

Morozova S (2020) Methylcellulose fibrils: a mini review. Polymer International 69(2):125–130

Onsager L (1949) The effects of shape on the interaction of colloidal particles. Annals of the New York Academy of Sciences 51(4):627–659

Paredez AR, Somerville CR, Ehrhardt DW (2006) Visualization of cellulose synthase demonstrates functional association with microtubules. Science 312(5779):1491–1495

Parvari G, Rotbaum Y, Eichen Y, Rittel D (2018) Impact-induced gelation in aqueous methylcellulose solutions. Chemical Communications 54(89):12578–12581

Reichler M, Rabensteiner S, Törnblom L, Coffeng S, Viitanen L, Jannuzzi L, Mäkinen T, Mac Intyre JR, Koivisto J, Puisto A, et al. (2021) Scalable method for bio-based solid foams that mimic wood. Scientific Reports 11(1):24306

Rezakhaniha R, Agianniotis A, Schrauwen JTC, Griffa A, Sage D, Bouten Cv, Van De Vosse F, Unser M, Stergiopulos N (2012) Experimental investigation of collagen waviness and orientation in the arterial adventitia using confocal laser scanning microscopy. Biomechanics and modeling in mechanobiology 11:461–473

van Roij R, Dijkstra M, Evans R (2000) Orientational wetting and capillary nematization of hard-rod fluids. Europhysics letters 49(3):350

Rosenmann ND, Irie LM, Korpanty J, Roth EW, Bleher R, Nupnar N, Wood K, Chen Y, Sumerlin BS, Weigand SJ, et al. (2026) Prediction of rheological properties via structure elucidation of solvated hydrogels. Nature Materials 25(6):1028–1036

Schindelin J, Arganda-Carreras I, Frise E, Kaynig V, Longair M, Pietzsch T, Preibisch S, Rueden C, Saalfeld S, Schmid B, et al. (2012) Fiji: an open-source platform for biological-image analysis. Nature Methods 9(7):676–682

Schmidt PW, Morozova S, Owens PM, Adden R, Li Y, Bates FS, Lodge TP (2018) Molecular weight dependence of methylcellulose fibrillar networks. Macromolecules 51(19):7767–7775

Tessari L, Cavezzi A, Frullini A (2001) Preliminary experience with a new sclerosing foam in the treatment of varicose veins. Dermatologic surgery 27(1):58–60

Thorkelsson K, Bai P, Xu T (2015) Self-assembly and applications of anisotropic nanomaterials: A review. Nano Today 10(1):48–66

Van der Walt S, Schönberger JL, Nunez-Iglesias J, Boulogne F, Warner JD, Yager N, Gouillart E, Yu T (2014) scikit-image: image processing in python. PeerJ 2:e453

Wicklein B, Kocjan A, Salazar-Alvarez G, Carosio F, Camino G, Antonietti M, Bergström L (2015) Thermally insulating and fire-retardant lightweight anisotropic foams based on nanocellulose and graphene oxide. Nature Nanotechnology 10(3):277–283

Wise HG, Takana H, Ohuchi F, Dichiara AB (2020) Field-assisted alignment of cellulose nanofibrils in a continuous flow-focusing system. ACS applied materials & interfaces 12(25):28568–28575

Supplementary Files

This is a list of supplementary files associated with this preprint. Click to download.

- MCNFAlignmentPaperSupplementary.pdf